Spinodal decomposition patterns in an isodensity critical binary fluid: Direct-visualization and light-scattering analyses

P. Guenoun, R. Gastaud, F. Perrot, and D. Beysens
Serivce de Physique du Solide et de Résonance Magnétique, Centre d'Etudes Nucléaires de Saclay, 91191 Gif-sur-Yvette Cédex, France
(Received 14 May 1987)

In order to study the phase-separation process near the critical point of fluid mixtures (spinodal decomposition) without the influence of the Earth's gravity, we have used a carefully density-matched system of deuterated cyclohexane, cyclohexane, and methanol. Such a system is known to behave as a real binary fluid [C. Houessou, P. Guenoun, R. Gastaud, F. Perrot, and D. Beysens, Phys. Rev. A **32**, 1818 (1985)], and our own previous microgravity experiments have demonstrated that the gravity influence was negligible during the whole separation. A light-scattering analysis has been performed, which provided the three-dimensional structure factor S mainly in the first stages of the separation. For the late stages a necessary alternative is the study of the images of the separating fluid. The interest of such a direct observation lies in the possibility of extracting not only statistical properties analogous to those obtained with the light-scattering technique, but also of analyzing the morphology of the phase-separation process and the motion of interfaces. The origin of such images is not straightforward. It is shown that they reproduce the section of the pattern of interfaces between phases, in a plane located close to the exit window. Because the domains are interconnected, and because only the interfaces nearly parallel to the light direction are detected, this pattern exhibits the same periodicity as that of the domains. From these images, a numerical treatment using video techniques and computer analysis allows a two-dimensional structure factor $\hat{S}$ to be obtained. The similarities and differences with the corresponding three-dimensional factor S are discussed. The scaling properties of the phase separation—the time invariance of the reduced structure factors F and $\hat{F}$, of the reduced second moments r and $\hat{r}$, the universal behavior of the typical wave vector K_m^*—can be verified in the whole available range, up to the final equilibrium state. Here wetting forces and the residual gravity effects compete to give to the system its equilibrium morphology.

INTRODUCTION

Suppressing convections and sedimentations during the phase separation of fluids systems may enable new growth mechanisms to be evidenced; this is one of the motivations for performing experiments in space, where the gravity level is near zero. An alternative way, which concerns the fluid-fluid phase separation, has been recently pointed out;[1] it involves a drastic reduction of the density difference of the fluid phases. This has motivated the work reported here, which deals with the new features appearing in the late stages of phase separation when the conditions of negligible convections and negligible sedimentation have been fulfilled.

For this purpose, we have elaborated a ternary liquid mixture (cyclohexane, deuterated cyclohexane, methanol) in order to match the density of the components as close as possible. This mixture was shown to behave as a real binary fluid with respect to its critical properties.[1] Such a method has enabled us to directly observe the stages of the phase separation which are usually dominated by gravity. The pattern due to spinodal decomposition could thus reach unusual macroscopic sizes, limited only by the finite size of the samples. The validity of such a phase separation as a simulation of a real microgravity environment has recently been checked;[2] we have performed two experiments in microgravity, using sounding rockets (Texus program), which have shown good agreement between our terrestrial results and those obtained under microgravity.

Phase separation in a critical binary fluid, more specifically the spinodal decomposition process, has been extensively studied by using light scattering techniques.[3,4] The most important result was probably the evidence of a scaled behavior of the phase-separation process, which was demonstrated via the experimental study of the structure factor. We present here a similar study which, however, takes advantage of a new analysis method: *the direct observation of the growth.*

This latter method indeed allows the study of the separation to be extended to the very late stages, owing to the analysis of the direct space patterns. For this purpose we discuss the formation of the optical image and its origin. The understanding of these optical conditions is essential to infer the statistical properties of the pattern, which enables the scaled behavior of the phenomena to be obtained (structure factor). Various comparisons can then be made with the corresponding light scattering data, keeping in mind that light scattering gives a three-dimensional (3D) analysis, whereas the images are of a two-dimensional (2D) nature.

This article deals with different problems, connected

either to the physics of the phase separation or to the comparison of this new image-analysis method with the classical light scattering techniques. For this reason we will describe in some details its organization.

Section I reviews the principal mechanisms involved in the phase separation of fluids, and especially the spinodal decomposition. Phase diagram properties (Sec. I A), different growth regimes (Sec. I B), and scaling properties (Sec. I C) are discussed.

In Sec. II the experimentally available observables are reported. After recalling the video system characteristics (Sec. II A), the light scattering observables, essentially the 3D structure factor S (Sec. II B), the direct observation of the phase separation pattern (Sec. II C) are discussed, image formation, quantitative analysis, and definition of a new structure factor $\hat{S}$. Then the relations between S and $\hat{S}$ are analyzed and a brief conclusion is given.

Section III deals with the experimental setup, and in Sec. IV we report the data corresponding to S (3D) and $\hat{S}$ (2D) and their scaling properties (Secs. II A and IV B). Especially a discussion of the behavior of a typical pattern size (L_m) is given in Sec. IV C. In Secs. IV D and IV E we take benefit of the visualization of the pattern to analyze the interface motion and the particular morphology of the spinodal-decomposition process. Finally, some comments are made.

I. SPINODAL DECOMPOSITION OF A CRITICAL BINARY FLUID

A. Phase diagram

The coexistence of the two phases of a binary fluid is schematically drawn in Fig. 1. In the plane [concentration (c)–temperature (T)], the curve (coexistence curve) characterizes the concentration of the phases at equilibrium. The top of the curve locates the critical point (c_c, T_c). The system is homogeneous in the region above the coexistence curve. The region below this curve is a region of nonstability, which can be divided into two domains according to the sign of the susceptibility $\chi=(\partial^2 F/\partial c^2)_{p,T}^{-1}$ where F is the free energy of the system.

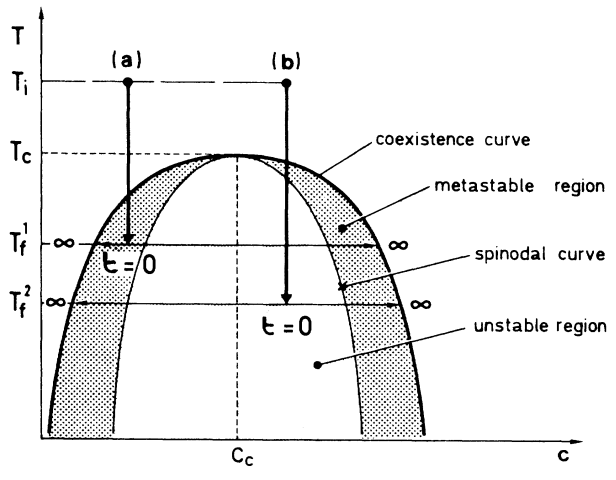

FIG. 1. Phase coexistence of a binary liquid mixture. c is the concentration of one of the components and T is the temperature. The system is monophasic above the coexistence curve and diphasic below. The spinodal curve separates the diphasic region into a metastable region and an unstable region. (a) and (b) represent thermal quenches in each of these regions.

A schematic way (Fig. 1) to investigate the mechanisms of phase separation is to quench the system from the one-phase region (temperature T_i) into the nonstable region (temperature T_f) and to study how the mixture relaxes towards equilibrium.

The initial regime (the "germination") is directly related to the sign of χ. In the domain where $\chi>0$ (the nucleation domain) the system is metastable, and only the fluctuations larger than a "critical radius"[5] are able to grow. In the domain $\chi<0$ (the spinodal domain) which is the only region that concerns a sample at criticality, the system is thermodynamically unstable; concentration fluctuations can grow and reach the equilibrium values.

Let us recall some classical critical properties which will be used in the following. Near the critical point, the system is characterized by the order parameter $M=c-c_c$ (we adopt the magnetic notation). The binary fluid concerning the static properties belongs to the same universality class as the three-dimensional Ising model. With the reduced temperature $\epsilon=(T-T_c)/T_c$, the correlation length ξ^- (in the two-phase region) behaves as

$$\xi^- = \xi_0^- (-\epsilon)^{-\nu} , \tag{1}$$

where ξ_0^- is the correlation length amplitude, which is system dependent, and ν is an universal exponent ($\nu=0.63$).

It is, however, generally the correlation length (ξ_0^+) which is determined in the one-phase region, and one has to apply the 2-scale-factor universality to infer ξ_0^-; according to a renormalization-group calculation,[6] $\xi_0^-/\xi_0^+=0.524$.

The surface tension σ between the two phases can be related to ξ^+ by using the following ratio from the 2-scale-factor universality:

$$\frac{k_B T}{\sigma} = R(\xi^+)^2 \simeq 4R(\xi^-)^2 , \tag{2}$$

where R has been experimentally found to be $R\simeq 2.6$.[7]

It is also useful to introduce the average lifetime τ^- of the fluctuations. This time can be understood as the typical Brownian diffusion time of a fluctuation of size ξ^-, and can be expressed as[8]

$$\tau^- = \frac{6\pi\eta}{k_B T_c}(\xi^-)^3 , \tag{3}$$

where k_B is the Boltzmann constant and η is the mean shear viscosity at the considered temperature.

The use of standard techniques (laser light scattering) enables the structure factor $S(K,t)$, i.e., the Fourier transform of the correlation function of the order pa-

rameter fluctuations, to be obtained via the scattered intensity[9]

$$I(K,t) \propto S(K,t) \propto \langle \, | \delta M_K(t) |^2 \rangle \, , \tag{4}$$

where K is the transfer wave vector and $\delta M_K(t)$ is an order-parameter fluctuation with same wave vector K.

B. The different regimes

Just after the thermal quench, the fluctuations are small. According to a *linear analysis* by Cahn,[10] one can write the time evolution of a fluctuation of wave number K as $\delta M_K = \delta M_0 e^{\omega(K)t}$. The growth rate $\omega(K)$ exhibits a peak at K_m (Fig. 2), and becomes negative for large values of K. This agrees with the intuitive finding that large K (small-sized) fluctuations, which correspond to high concentration gradients and are costly in energy, must disappear; and that small-K (large-sized) fluctuations, which involve weak concentration gradients, should grow with a very small rate.

The modes around K_m dominate the growth, imposing a characteristic quasiperiodic interconnected pattern of typical wavelength $L_m = 2\pi/K_m$. A numerical simulation is presented in Fig. 3.

Nonlinearities, which are due to the coupling of modes, complicate the simple scheme previously described, and prevent it from being confirmed experimentally. One of the new main features which emerge is the time dependence of K_m which decreases with time. Langer *et al.*,[11] neglecting the hydrodynamic degrees of freedom, have found a power-law variation $K_m^{-1} \propto t^a$ with $a \sim 0.2$. The behavior of $I(K,t)$ is indeed no longer exponential with time, as saturation of the growth occurs. A qualitative understanding of this effect is given in Fig. 4, where the growth of a fluctuation up to the local equilibrium is illustrated.

Kawasaki and Ohta[12] have extended Langer's ideas to

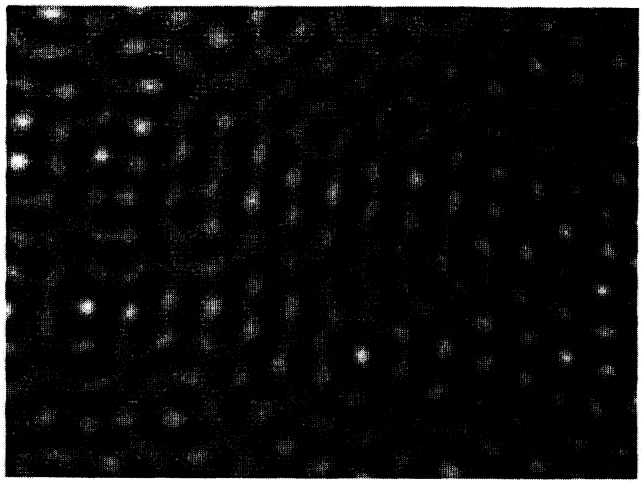

FIG. 3. Numerical simulation of a spinodal decomposition pattern. 20 modes of wavelength having random directions (uniform angular distribution between 0 and 2π), random phases (uniform distribution between 0 and 2π), and random amplitudes according to a Gaussian distribution (64 levels), are added.

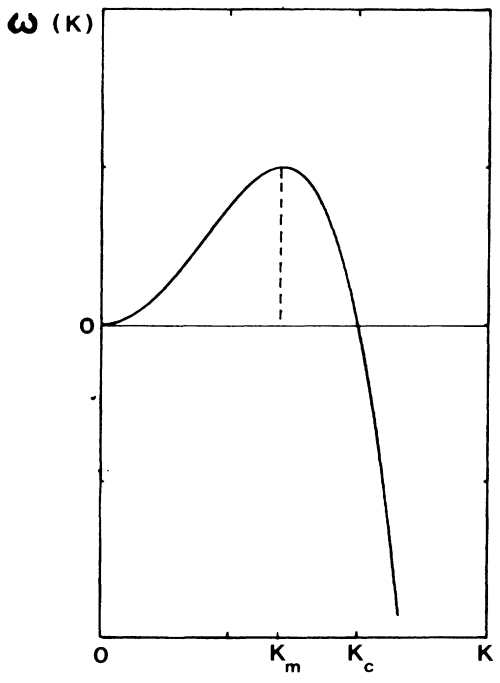

FIG. 2. Amplification factor $\omega(K)$ vs the wave vector K. Following the linear theory, $\omega(K)$ is positive for $K < K_c$ and exhibits a maximum at $K = K_m$.

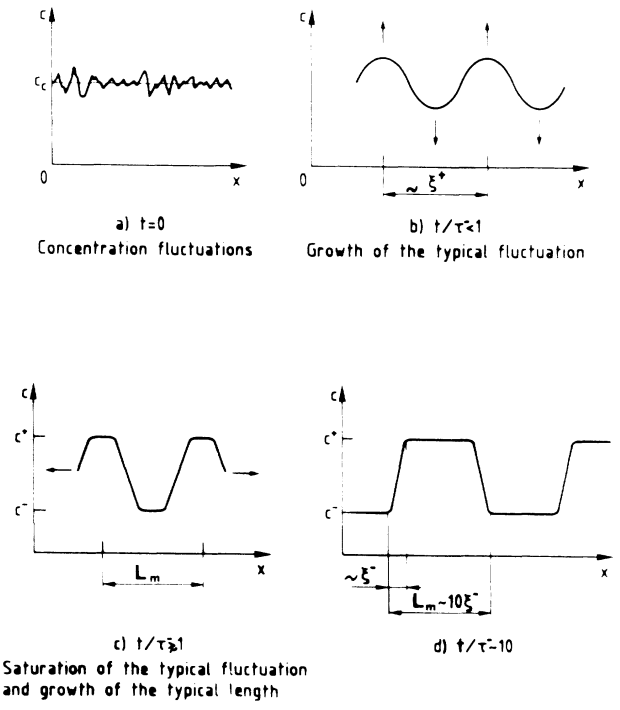

FIG. 4. Illustration of the growth of fluctuations in the early stages of the spinodal decomposition.

binary fluids but none of the authors have been able to completely describe the late stages. In these stages, where well-defined interfaces between domains are established, the influence of the surface tension becomes important. A crossover towards a $K_m^{-1} \propto t$ behavior was qualitatively explained by Siggia[13] and Cahn and Moldover[14] as a growth due to capillary flows.

On the basis of a new dynamical interfacial model, Kawasaki and Ohta[15] have identified all the processes encountered during the spinodal decomposition in fluid mixtures. In this model they assume that the local equilibrium has been reached. Here the local concentrations are those determined by the coexistence curve. This occurs typically for times $t \sim \tau^-$ (see Sec. II D below).

For the typical length L_m, they have obtained the two main behaviors $L_m \propto t^{1/3}$ and $L_m \propto t$. The latter accounts for hydrodynamical effects, and the $\frac{1}{3}$ power law corresponds to the diffusion-reaction process, the coalescence of domains being activated by their Brownian motion (see also Ref. 16). The growth of $L_m(t)$ is thus explained by the coarsening of the domains which increase their mean size. This coarsening probably leads to the change of the morphology of the two phases. For instance, the picture in Fig. 3 would be modified by a breakup of the connectivity of the phases. One can then suggest that a complete description of the problem would involve other quantities besides $L_m(t)$. In addition to $L_m(t)$, which can always be understood as the mean spacing between domains, the mean size of the domains $R(t)$, and their polydispersity would be relevant.

Up to now gravity g has been neglected. However, gravity can induce also a new crossover, towards a regime dominated by convection and sedimentation flows. The denser phase sinks down and the lighter rises up. Simple arguments, as developed by Siggia,[13] show that the crossover takes places when the size of the domain is comparable to the capillary length

$$l_c = \left[\frac{\sigma}{g \, \Delta\rho} \right]^{1/2} , \tag{5}$$

where $\Delta\rho$ is the density difference of the two phases at the temperature T_f, i.e., when

$$K_m l_c \lesssim 1 . \tag{6}$$

This condition can be easily verified experimentally.

Finally, the growth will stop when the domain size becomes comparable to the sample size (e), or when

$$K_m e \sim 1 . \tag{7}$$

If therefore one wants to suppress the gravity influence in the phase-separation process, one needs, at least, to fulfill both (6) and (7), i.e., to make the capillary length of the order the sample size, that is,

$$l_c \sim e . \tag{8}$$

Finally, we note that when a macroscopic size is obtained, finite size effects will arise, including wetting phenomena. They will introduce an asymmetry between the phases, since one phase will preferentially wet the walls of the cell.[17] In the absence of any gravity influence, wetting forces should control the final equilibrium state of the system. For instance, near a critical point, a macroscopic wetting film can be observed.

C. Scaling properties

The scaling idea was originally introduced by numerical simulation[16,18] and also confirmed experimentally.[3,4] Only one length scale (L_m) appears to be relevant, and physical quantities should depend on time only through this length scale.

Experimentally the main points which have been investigated are the following:

(i) The scaling behavior of $S(K,t)$ can be tested through the possible time independence of a reduced structure factor[18]

$$F(x,t) \equiv \frac{K_m^3 S(K,t)}{\int_{K_A \ll K_m}^{K_B \gg K_m} S(K,t) K^2 \, dK} , \tag{9}$$

where $x = K/K_m$.

This reduced structure factor is dimension dependent. In the following, we will have to deal with a 2D pattern, with a structure factor $\hat{S}(K,t)$, whose corresponding reduced factor $\hat{F}(K,t)$ can be deduced through

$$\hat{F}(x,t) = \frac{K_m^2 S(K,t)}{\int_{K_A \ll K_m}^{K_B \gg K_m} S(K,t) K \, dK} . \tag{10}$$

(ii) Another test of the scaling is the study of the ratio defined as a reduced second moment of the intensity[18]

$$r(t) = \frac{k_2(t)}{k_1^2(t)} , \tag{11}$$

where $k_n(t)$ is the intensity moment of order n defined by

$$k_n(t) = \frac{\int K^n S(K,t) dK}{\int S(K,t) dK} . \tag{12}$$

A perfect scaling behavior would imply that these two quantities do not vary during all the phase separation.

(iii) The characteristic length of the system, $L_m(t)$, is commonly understood as a measure of the periodicity of the ordered regions which are developing in the system.

Note that light scattering experiments give the opportunity of deducing $L_m(t)$ from $S(K,t)$. Although the first moment $k_1(t)$ is often related to $L_m(t)$ in theoretical works, the most natural choice which is offered to the experimentalist is the maximum of $S(K,t)$, which is precisely the average distance between the domains according to the theory of light diffraction.[19]

In reduced units, the dimensionless wave vector $K_m^* = K_m \xi^-$ versus the reduced time $t^* = t/\tau^-$ exhibits a universal behavior

$$K_m^* = f(t^*) , \tag{13}$$

where f is system independent.

The scaling approach enables the behavior of the above quantities to be determined through the following:

(i) A reduced structure factor $F(x)$. One has to consider two asymptotic behaviors, namely, $x \ll 1$, where the local mass conservation implies $F(x) \sim x^2$ and $x \gg 1$, where a Porod law modified by the domains connectivity leads to $F(x) \sim x^{-6}$.

Furukawa[20] has proposed an expression compatible with these conditions,

$$F(x) = 4x^2/(3+x^8) . \tag{14}$$

(ii) A universal curve $K_m^* = f(t^*)$. Considering the two asymptotic behaviors $K_m^* \sim (t^*)^{-1/3}$ and $K_m^* \sim (t^*)^{-1}$ Furukawa[20] has obtained, for the characteristic length $L_m^* = (K_m^*)^{-1}$, the relation

$$\frac{dL_m^*}{dt^*} = A^* (L_m^*)^{-2} + B^* \tag{15}$$

with two adjustable parameters A^* and B^*. By integration and using the initial condition ($L_m^* = 1$ for $t^* = 0$), (15) becomes

$$(L_m^* - 1) - \left[\left(\frac{A^*}{B^*} \right)^{1/2} \left\{ \tan^{-1} \left[L^* \left(\frac{B^*}{A^*} \right)^{1/2} \right] - \tan^{-1} \left[\left(\frac{B^*}{A^*} \right)^{1/2} \right] \right\} \right] = B^* t^* . \tag{16}$$

Note that in all these predictions only the critical region is concerned and that the gravity effects are neglected.

II. OBSERVABLES

The main interest of using an isodensity system lies in the possibility of studying directly the *morphology* of the phase separation, and not only properties already averaged. This has lead us to set up a video system allowing a direct observation of the sample to be made, with structures typically in the range $L_m = 10-10^4$ μm according to the magnification rate used.

In order to interpret the morphology in the same terms as the previous light scattering studies, we have also performed scattering experiments. In place of the direct image, we have recorded, by video, the scattered light pattern. A typical range is $L_m = 3-30$ μm, and it is therefore mainly in the early stages of phase separation that this technique has been applied.

Let us first describe the video system.

A. Video system characteristics (Ref. 21)

The video system consists of a video camera, videotape and a computer.

The video camera includes a 1-in Newicon tube, of sensitivity 0.1 lux. The fact that the electron beam needs a time $t_0 = 40$ ms to reset a pixel (i.e., picture element) implies that the information in each point is integrated over t_0.

The pictures are stored on a videotape (U-matic $\frac{3}{4}$ inch), then digitized on 256×256 pixels and 6 bits (64 levels) on a computer. The method of sampling is such that the information in each pixel is in fact averaged over a quarter of a pixel area.

The camera and the digitization processor have been tested in order to check the linearity in intensity and also the spatial homogeneity of the pattern. These latter are of order 1% in the central part of the picture.[21] Only the central part (128×128 pixels) of the pattern is analyzed.

B. Light scattering

A typical pattern of light scattering consists of a spinodal decomposition ring (Fig. 5). Once digitized, this ring is fitted to determine its center and its diameter ($2K_m$). Due to the symmetry, a radial average of the intensity is then performed and the intensity versus the scattering angle $I(\theta,t)$ is obtained. It is finally converted to $I(K,t)$.

Let us examine in greater detail the link between such a measurement and the structure factor $S(K,t)$. The latter is computed as

$$S(K,t) = \langle \, | \delta M_K(t) | \, ^2 \rangle_0 , \tag{17}$$

where $\delta M_K(t)$ is regarded as a stochastic variable connected to a probability distribution functional $P(M,T)$. $\langle \, \rangle_0$ then denotes an average over P.

$I(K,t)$ is also an average of $| \delta M_K(t) |^2$ that we will examine in more detail:

(a) The first average which has to be estimated is made over the scattering volume Vs. The problem reduces to evaluating how many domains can be considered in the cross section a of the laser beam. This number is of order $a^2/L_m^2 \simeq a^2/(4\pi^2)K_m^2$ and remains in the range 80–800 for the typical values $a \simeq 200$ μm and $K_m = 2000-20\,000$ cm^{-1}.

An equivalent formulation is to consider the number of coherence areas summed up on the observation screen to obtain the information related to an angle θ. Since radial symmetry is observed, a radial average can be

FIG. 5. Typical spinodal decomposition ring obtained by light scattering 70 s after the beginning of the quench ($T_c - T_f = 3$ mK, $K_m = 3.8 \times 10^3$ cm^{-1}, C^*C-M system).

realized over the spinodal ring. It covers typically 100 coherence areas.

This radial average gives $\langle |\delta M_K(t)|^2 \rangle_1$. We have noted the subscript 1 to recall that this average is different from the above average $\langle \ \rangle_0$ which had to be made on a set of equivalent systems. However, in the limit where the coherence areas can be considered as statistically independent, and that 100 areas is a sufficiently large statistical set, one can consider both averages as being equivalent.

(b) The temporal integration of the picture over $t_0=40$ ms would provide an average of the intensity if $t_0 \gg \tau^-$, the typical lifetime of a fluctuation. However, typically $T_c - T_f \sim$ a few mK, thus $\tau^- \sim 300$ ms. This shows that the video scanning does not provide any time average on $I(K,t)$.

(c) The digitization of the picture could lower the angular resolution. This loss of resolution does not introduce any problems, because the range of interest is always much larger than one pixel. We can therefore conclude that the mean value $I(K,t)$ which is computed via the video system is correctly related to the structure factor $S(K,t)$.

C. Direct observation

1. *Image formation*

A digitized picture of the structures obtained in real space is shown in Fig. 6. A good contrast is obtained only when the focus is done on a plane which is close to the exit inner plane of the cell (Fig. 7), more precisely at a distance of order L_m.

This seems to be very natural as the superposition of the structures between the exit plane and the focus plane makes the picture very fuzzy if the latter is located too deep within the bulk.

An important point is now to elucidate the meaning of patterns such as Fig. 6. It is tempting to interpret this picture as the exact replica of Fig. 3, the dark domains identifying one phase and the bright domains the other. However, such a picture can have many origins, and in the following we review different possibilities.

(a) Transmission? The first interpretation could be due to a difference in *transmission,* itself due to a difference in turbidity. The turbidity can be evaluated for both phases at equilibrium as[22]

$$\mathcal{A}=\frac{\pi^2}{\lambda_0^4}\left[\frac{\partial n^2}{\partial c}\right]^2 S_n^2 G(\epsilon, K_0\xi^-) \ . \tag{18}$$

Here λ_0 is the wavelength of light in a vacuum and $K_0=2\pi n/\lambda_0$ is the light wave vector in a medium of refractive index (n). The function (G) and the derivative $(\partial n^2/\partial c)$ are identical for both phases, so the variations of $\mathcal{A}$ have to be attributed only to the local field factor S_n. In fluids the Yvon-Vuks formulation[23]

$$S_n=\frac{9n^2}{(n^2+2)(2n^2+1)} \tag{19}$$

is seen to describe well the experimental data. This allows the transmission variation corresponding to a refractive index variation Δn to be evaluated. Using the definition of the transmission factor,

$$\mathcal{T}=\exp(-\mathcal{A}e) \ , \tag{20}$$

the corresponding variation can be calculated using the numerical values of Ref. 1 for a typical quench of 10 mK. In particular, the refractive-index difference between the two phases is

$$\Delta n \simeq 5\times 10^{-3} \ ,$$

which leads, for a sample thickness $e=0.2$ cm, to a vari-

(a)

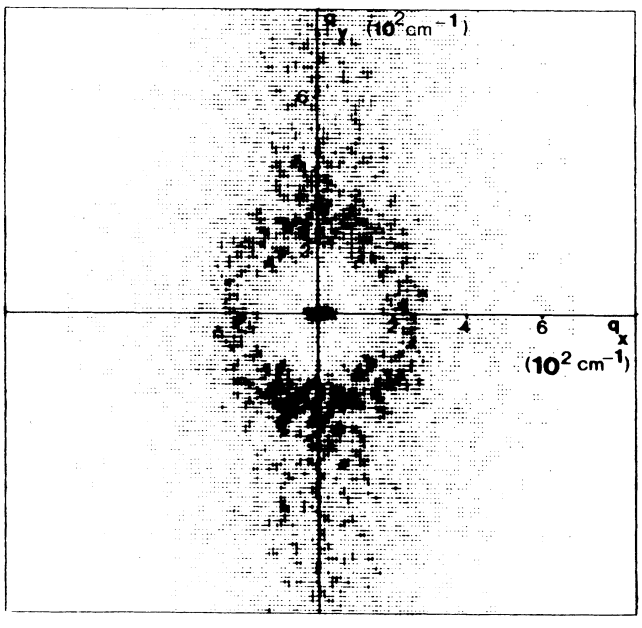

(b)

FIG. 6. (a) Spinodal structures obtained by direct observation. This picture is digitized here only on 5 levels. (b) Structure factor $(\hat{S})$ computed from the structures (a). The radial symmetry is confirmed in spite of a slight asymmetry due to the digitization.

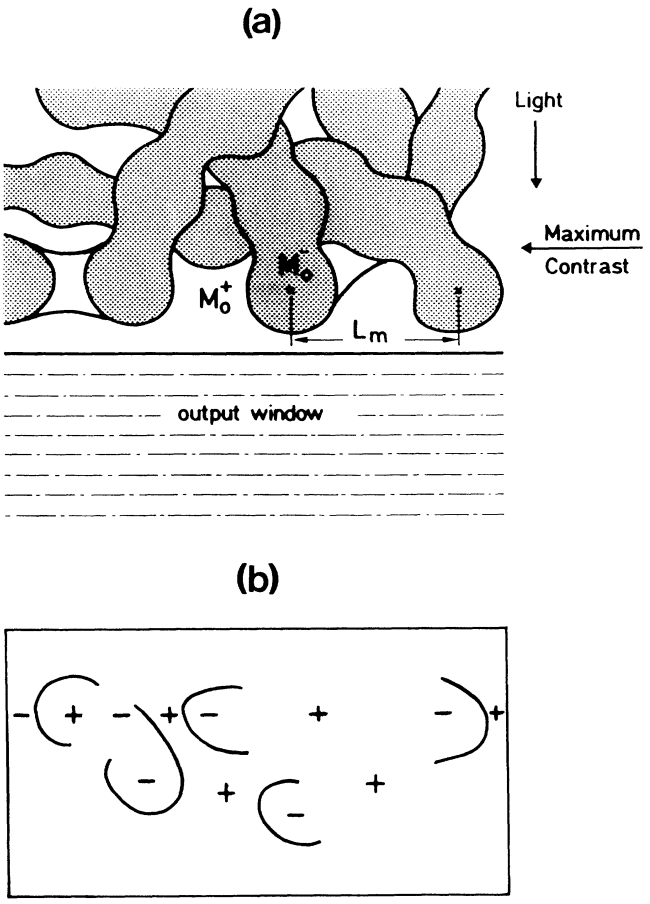

FIG. 7. Phase separation in the vicinity of a window. M_0^+ is the wetting phase and M_0^- the nonwetting phase. The approximate location of the plane of maximum contrast is indicated. (a) Front view; (b) top view.

ation $\mathcal{T} \simeq 5 \times 10^{-4}$. This transmission variation is clearly too small to account for the highly contrasted pattern which has been observed.

(b) Schlieren? An object which is formed of a refractive-index modulation is classically detected through coherent illumination by Schlieren optics.[24] This is nothing more than the suppression of $K \simeq 0$ modes in the Fourier space of the optical device in order to consider only the $K > 0$ modes.

In the range $L_m = 10-100$ μm, the sample is very turbid because of the vicinity of the critical point. Therefore, schlieren is not very efficient at this stage. We have checked this point by transforming the setup into a schlieren device, adding a mask (M) in the focal plane of the observation lens (L_4) (see Fig. 11). In the range $L_m = 10^3-10^4$ μm, schlieren becomes efficient in increasing the contrast of the interfaces between the two phases.

(c) Self-focusing? The domains can also be considered as an ensemble of spherical diopters, which separate two phases of different refractive indices and which focus the incident light (Fig. 7). An order of magnitude of the corresponding focal length is $L_m/(4\Delta n) \simeq 50 L_m$, which is always much larger than L_m. The intensity variations connected to this convergence effect remain therefore negligible.

(d) Interface scattering? The observations are concerned with a time region where the size of the domains is much larger than the light wavelength. These domains are very poor scatterers. This is not the case for their mutual interfaces, of order of a few correlation lengths. The visualization of the domains will therefore mainly be performed through the light scattered by these interfaces.

In Fig. 8 we show some pictures corresponding to 3 typical scales. It is clear that a mere change of scale makes the image 8b, in the range 10^2-10^3 μm, similar to

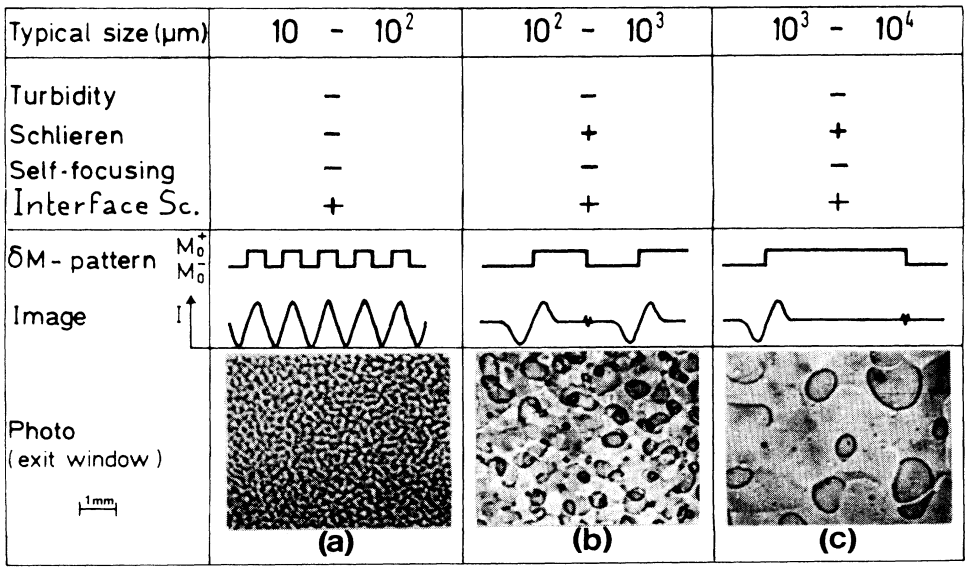

FIG. 8. Presentation of the various optical conditions encountered during the phase separation. For each size the respective influence of the mechanisms is listed, from − (low efficiency) to + (high efficiency).

the image 8(c) in the range 10^3-10^4 μm, in agreement with the expected scaling properties of the phase-separating pattern. However, Fig. 8(a) in the range $10-10^2$ μm seems to exhibit a different morphology. This paradox disappears when the limitations due to the optical resolution of the instruments are taken into account. One indeed easily realizes that 8(a) can be reconstructed from 8(b) by a mere change of scale plus an enlargement of the black and white lines which denote the location of an interface. This phenomenon is also responsible for the apparent larger contrast in the smallest length range.

The effective depth of field in the focusing plane is determined by the resolution, i.e., by the aperture number of the lens (here close to F:1). For instance, the minimum resolution available in Fig. 8 corresponds to about 50 μm.

The signature of an interface is mostly, as reported in Fig. 8, a dark line followed by a bright line. A few events, connected to slight defocusing effects, are also visible, bright line or dark line. An important remark has to be made: only the interfaces perpendicular or nearly perpendicular to the focusing plane will become visible (cf. Fig. 7). For sake of simplicity, we will assume that statistically, only half of the interfaces will be therefore detected. This makes the visible interfaces have the same periodicity as the domains, and not the half period. This property is due to the nonspherical shape of the domains, and ultimately to their interconnectivity. On the contrary, the interface pattern of spherical droplets gives rise to a typical periodicity which is half of the droplet periodicity. This has been checked experimentally.

2. *Pattern analysis*

There are several steps in the analysis of such a picture.

(a) Image modeling. The image on the video camera (axes x,y) is a time-dependent two-dimensional image of intensity $I(x,y,t)$. As noted above, this intensity can be related to the location of an interface nearly parallel to the light $[i_{\parallel}(x,y,t)]$, in a section near the exit window with a depth of order L_m. Strictly speaking, one has to consider the image as the convolution of $i_{\parallel}$ by the instrumental function $\mathcal{F}(x,y)$,

$$I(x,y,t)=i_{\parallel}(x,y,t)\otimes\mathcal{F}(x,y)+A(t)\ . \tag{21}$$

The parameter $A(t)$ represents a continuous background, which varies with time. In contrast to the light scattering technique, one notes that the quantity I is already spatially averaged, at least over the size of a pixel, which is always larger than ξ^-.

(b) Quantitative analysis of the pictures: the structure factor. The typical size (δl) related to a pixel is, according to the optical magnification, in the range $\delta l=1.5-80$ μ m. The time evolution of the pattern is always much larger than the scanning time of the video camera (40 ms) thus making the corresponding time averaging negligible.

In order to obtain the structure factor of this pattern, it is necessary to perform a numerical Fourier transform of the digitized intensity $[I(\mathbf{K}_i,t)]$ and to compute the square of its modulus $[\,|I(\mathbf{K}_i,t)|^2]$ where i is an index running from 1 to 128×128, which denotes each pixel. The structure factor exhibits a radial structure (Fig. 6), which makes it very similar to the usual light scattering ring (Fig. 5). Finally, a radial average as described above in Sec. II B is performed, allowing the quantity $\hat{\sigma}(K_i,t)$ to be obtained (here $K_i=|\mathbf{K}_i|$),

$$\hat{\sigma}(K_i,t)=\langle\,|I(\mathbf{K}_i)|^2\rangle_1 \tag{22}$$

or

$$\hat{\sigma}(K_i,t)=|\mathcal{F}(K_i)|^2\langle\,|i_{\parallel}(K_i,t)|^2\rangle_1+B(t)+|A(t)|^2\delta(K_i)\ . \tag{23}$$

The average $\langle\ \rangle_1$ has the same meaning as that obtained with light scattering experiments (see Sec. II B), and the same limitations. Especially the number of interfaces in the picture should remain large enough to ensure that a statistical average is really performed. The background $B(t)$ is connected to the digitization of the image, and $|A|^2\delta(K_i)$ represents the initial background. It is clear that a more rigorous treatment taking into account the discretization of the image and the finite numbers of pixels can be performed, making visible a minimum spacing $\delta K\sim1/(128\delta l)$ and a maximum range $\Delta K\sim1/\delta l$.

The function $\hat{\sigma}$ will therefore reproduce the structure factor of the interface position to within the approximation of the $|\mathcal{F}|^2$ factor. This factor is only optics dependent, and will be made equal to unity in the following, which means that the magnification rate and the resolution of optics have been correctly chosen.

Finally, another limitation arises from the small number of interfaces in the picture; typically any statistical analysis becomes meaningless when less than seven interfaces remain in the pattern, which corresponds to a minimum wave vector $K_M^0\sim50$ cm^{-1}. There is, moreover, a region where the $|A|^2$ term is so large that it is difficult to separate a structure from the central peak.

If one can reasonably claim that the measurement of $\hat{\sigma}$ allows, by substracting a background B and a $K=0$ peak A, the interface structure factor $\langle\,|i_{\parallel}(K_i,t)|^2\rangle_1$ to be inferred, it is worth noticing that one cannot compare it directly to the usual three-dimensional structure factor of the domains as obtained by light scattering. Their origins are different. This is why we will note in the following the structure factor obtained from a two-dimensional picture as

$$\hat{S}(K_i,t)\simeq\langle\,|i_{\parallel}(K_i,t)|^2\rangle_1\ . \tag{24}$$

Nevertheless, in Sec. II D we will develop reasonable arguments which justify high similarities between S and $\hat{S}$. Experimental results (see Sec. IV) will moreover confirm such a resemblance.

(c) Other typical parameters. New informations—new observables—can also be obtained without performing a Fourier transform of the pictures. For instance, the characteristic length (L_m) can be estimated directly

from a digitized picture. And the motion of an interface can be studied from the direct observation, allowing a typical interface velocity to be obtained and compared to the estimations (see below).

D. Relation between S and $\hat{S}$

The comparison between S and $\hat{S}$ needs a model. We will describe a very natural model, based on the assumption that the local equilibrium between the phases is reached just after the quench, after a time $t^* \sim 1$.

1. *The structure factor of the 3D pattern*

Several arguments can be given to justify the assumption of local equilibrium. First, rough calculations can be done by using Cahn's model to estimate the time necessary to reach the local equilibrium. In so doing one gets, for instance, $t^* \sim 20$ in the case of a quench depth of $2mK$. Also numerical simulations performed with pure fluids indicate that the Cahn regime has finished when $t^* \sim 8$.[25]

More convincing arguments are provided by experiments concerned with the phase separation of a critical binary fluid which relaxes towards equilibrium after having been stirred in the two-phase region.[26] Stirring homogenizes the mixture by turbulence at a scale of order a few μm, a scale where the initial equilibrium concentrations should be preserved. The structure-factor evolution of such a system being identical to that obtained after a thermal quench, the above assumption about the rapid attainment of the local equilibrium seems, therefore, well supported.

Once this local equilibrium is assumed, we can use a description of the order-parameter field already used by Ohta,[27]

$$M(\mathbf{r},t)=M_0 \mathrm{sgn}[u(\mathbf{r},t)]+\delta M(\mathbf{r},t) \ . \tag{25}$$

The function $\mathrm{sgn}(x)$ is a function whose value is ± 1 if x is positive or negative; $\pm M_0$ is the equilibrium value of the order parameter at T_f and $u(\mathbf{r},t)$ is a field which specifies the location of the interfaces between the domains: $u(\mathbf{r},t)=0$ for $\mathbf{r}$ corresponding to an interface, $u>0$ or $u<0$ if $\mathbf{r}$ belongs to the phase $(+M_0)$ or $(-M_0)$, respectively. The formulation (25) remains valid in the approximation $t^* \gg 1$ (local equilibrium) and $K\xi^- \ll 1$ (interface profile neglected).

The structure factor of such a concentration field can be written as

$$\begin{aligned} S(K,t)=\langle M_0^2 \mid s_K(t) \mid^2 & \\ +M_0[s_K(t)\delta M_K^*(t)+s_K^*(t)\delta M_K(t)] & \\ + \mid \delta M_K(t) \mid^2 \rangle_1 \ . & \end{aligned} \tag{26}$$

The factor $s_K(t)$ is the Fourier transform of the function $\mathrm{sgn}[u(\mathbf{r},t)]$, and δM_K is the Fourier transform of $\delta M(\mathbf{r},t)$ (the superscript asterisks denote the conjugate part of these quantities).

In the limit $K\xi^- \ll 1$, several approximations can be performed. First, the structure factor of the fluctuations can be expressed by its $K=0$ value, i.e., the susceptibility χ^-,[8]

$$\langle \mid \delta M_K(t) \mid^2 \rangle_1 \simeq \chi^- \ . \tag{27}$$

There are no reasons to assume correlations between the fluctuations δM and the interface pattern; therefore the average (26) can be simplified to

$$S(K,t)=M_0^2 \langle \mid s_K(t) \mid^2 \rangle_1 + \chi^- \ . \tag{28}$$

If we leave out the constant term χ^-, this structure factor provides a description of the organization of the 3D pattern via s_K. (An example of calculations for spherical domains can be found in Ohta.[27]) And the scaling of $S(K,t)$ will express the scaled behavior of the morphology of the domains as the phase separation proceeds.

One notes finally that the function $\mathrm{sgn}(u)$ varies only at the domain interfaces. Thus the Fourier transform (s_K) is also closely related to the structure factor of the interfaces.

2. *The structure factor of the direct observation pattern*

The image which is detected can be considered as the section of the 3D pattern at a distance $\sim L_m$ from the exit window. A first question is what is the precise influence of the wall on the morphology of the structures?

Complete wetting of one phase[17] is seen near T_c. This implies the existence of a wetting film of one phase (M^+ phase) on the wall. Provided that the longitudinal extension of this film is smaller than the location of our focus plane, the influence of the wall on the interface pattern must remain negligible (Fig. 7).

A second question concerns the nonvisualization of interfaces which are not approximately perpendicular to the plane of observation. This phenomenon reduces in fact the number of visible interfaces by roughly a factor of 2 and, provided that statistics can apply, it seems reasonable to assume that the consequences on the structure factor are negligible. One, however, notices that this has the nice consequence of giving the same typical frequency as the domains. This frequency should have been the double if all interfaces have become visible, an interface M_0^+-M_0^- giving rise to the same intensity peak as an interface M_0^--M_0^+.

Keeping in mind all these approximations, one realizes that it is therefore the structure factor of interfaces between the domains of a section of the phase-separating pattern that we determine through $\hat{S}(K,t)$.

3. *Final remarks*

A more quantitative analysis of the relations between the structure factors S of the domains and $\hat{S}$ of the interfaces is beyond the present study. However, S and $\hat{S}$ must show strong similarities. In particular, the information they provide are of the same kind, in the sense that they reproduce the Fourier spectrum of the distribution of domains, or of detected interfaces between domains. Therefore the scaling properties should be the

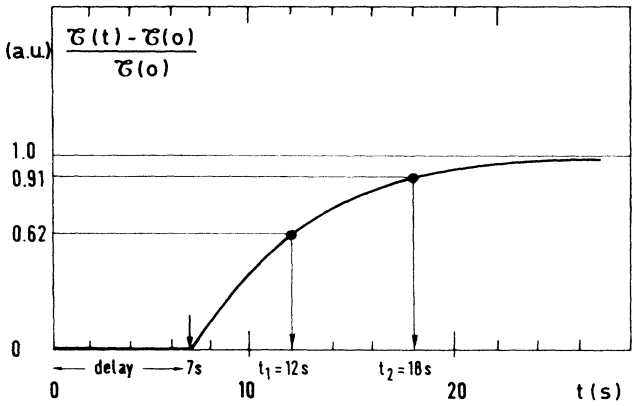

FIG. 9. Experimental determination of the time delay during a quench performed with T_i and T_f in the monophasic region using light transmittency ($\mathcal{T}$). The delay is chosen as the time where $[\mathcal{T}(t)-\mathcal{T}(0)]/\mathcal{T}(0)=0.62$.

same, and more specifically, the periodicity K_m will be reproduced in both S and $\hat{S}$. The exact shapes cannot be compared directly, the 2D interface morphology being only similar, and not identical, to the 3D pattern case. The experimental results (see below, Sec. IV) will demonstrate strong similarities between S and $\hat{S}$; surprisingly, the shapes themselves will be found to be very similar.

III. EXPERIMENTAL

The system which was used was, in fact, a ternary mixture whose components are cyclohexane (C) with a small amount of deuterated cyclohexane (C^*) and methanol (M). This mixture was fully studied in a previous paper[1] where its critical properties were investigated. In particular, it has been shown that this mixture behaves as a real binary fluid with reference to the shape of the coexistence curve and to the various critical parameters.

With m_x the mass of the component x, the different ratios which have been used are the deuteration ratio

$$c_0=\frac{m_{C^*}}{(m_C+m_{C^*})}\simeq 3\%$$

and the critical mass fraction

$$c_C=(m_C+m_{C^*})/(m_C+m_{C^*}+m_M)=0.76\pm 4\times 10^{-3}\ .$$

At $T_c-T_f=10$ mK, a typical value for the difference in density between the two separating phases at equilibrium is $\Delta\rho\simeq 10^{-6}$ g cm^{-3}. This latter value was obtained from the measurement of the Laplace length [see Eq. (5)].

It is for a deuteration ratio close to 3%—and varying from 2% to 4% under the influence of uncontrolled impurities—that the Laplace length was the largest, of order of the sample size. As noted above in Sec. I, this observation was a necessary condition to suppress the gravity effects during all the phase separation [Eq. (8)].

The cells are made of quartz, of cylindrical shape, with an inner diameter of 2.0 cm and inner thickness 0.200 cm. The observation windows are optically flat. Cells are filled through a 5-mm quartz pipe which was then sealed by a Teflon stop. They are quite identical to those used in the microgravity experiments; a full description can be found in the corresponding reports.[1,2]

The sample cell was immersed in a water bath with thermal regulation of ± 0.2 mK near $T_c\simeq 45$ °C. The quench was performed from a temperature T_i close to T_c $[T_i=T_c+(0.5-5)$ mK] to T_f below T_c $[T_f=T_c-(0.5-15)$ mK], by means of a heat exchanger working during a calibrated time period. The time response of the bath plus the sample has been studied using the light transmittency in the mixture itself, in the homogeneous region $T>T_c$. A detailed analysis is reported in Fig. 9,

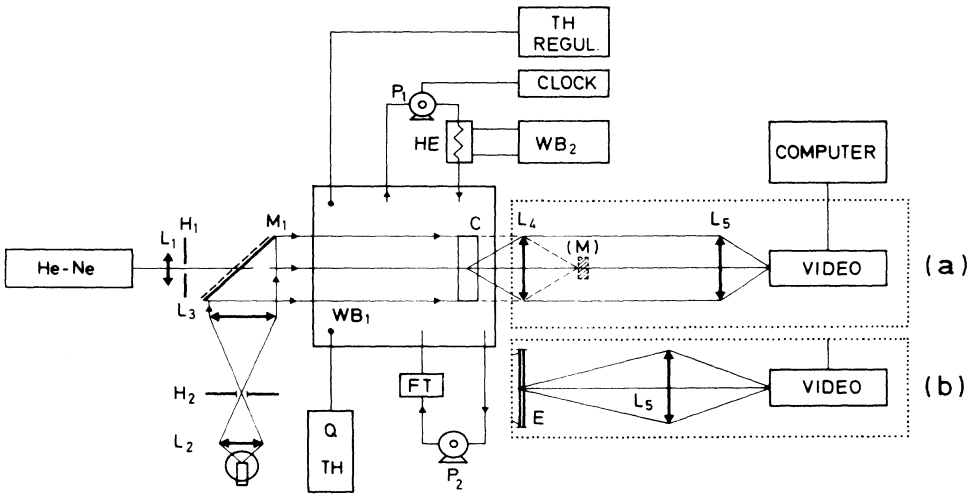

FIG. 10. Experimental setup used for both direct observation (a) and light scattering (b). L_1,L_2,L_3,L_4,L_5, lenses; He-Ne, helium-neon laser; H_1,H_2, pin holes; M_1, semitransparent mirror; Qth., quartz thermometer; WB_1,WB_2, temperature-regulated water baths; P_1,P_2, pumps; FT, water filter; HE, heat exchanger; C, cell; M, mask, E, screen.

where we see that the dead time is approximately 12 sec.

The general setup derives from that already used in Ref. 1. It is reported in Fig. 10. It can be used either as a light scattering setup [Fig. 10(b)] when illuminating the cell with a slightly focused He-Ne laser beam of a few mW power, or as a direct-observation optical device, when illuminating the sample by collimated white light [Fig. 10(a)].

The early stages of the phase separation can be better studied by light scattering (range $K_m^* \sim 0.1-1$), whereas the late stages are chiefly concerned with the direct space observation. There is obviously a region of overlap, which is of prime importance for checking the assumptions concerning the two different structure factors S and $\hat{S}$, as defined in Sec. II.

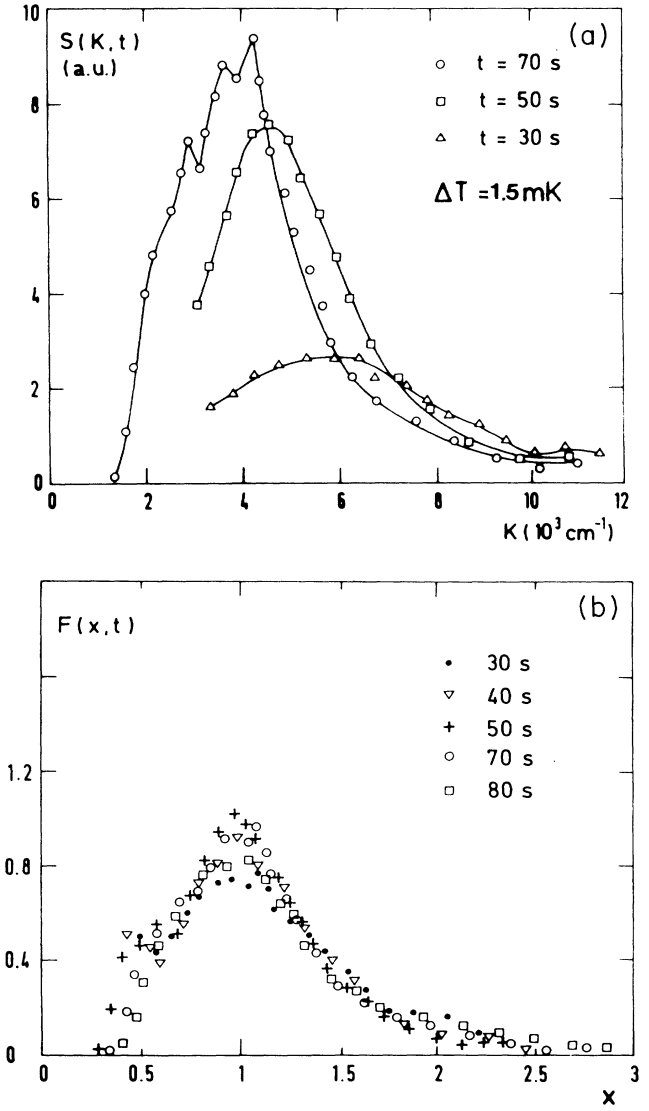

FIG. 11. (a) Typical temporal evolution of $S(K,t)$ for a 1.5-mK quench depth (light scattering). (b) Scaling function $F(x,t)$ corresponding to the evolution shown in (a). The times are those corresponding to the symbols on the figure.

The typical range that can be covered by light scattering is $K_m = 2000-20\,000$ cm^{-1} or $L_m = 3-30$ μm; different magnification ratios allow direct space structures to be investigated in the range $L_m = 10-20\,000$ μm.

In Sec. II A we have already described the characteristics of a digitized picture and how the averages have to be accounted for.

Specific softwares[21] have been elaborated to compute the structure factor $S(K,t)$ from the light scattering measurements (determination of the ring center, radial average) and to determine the structure factor $\hat{S}(K,t)$ from the direct-observation pattern (fast Fourier transform, radial averages).

Finally, the scaled forms $F(x,t)$ and $\hat{F}(x,t)$, and the ratios $r(t)$ and $\hat{r}(t)$ are computed from, respectively, S and $\hat{S}$ according to the expressions (9) and (10). Practically the limits of the involved integrals have been taken as

$$K_A = K_m/2 \text{ and } K_B = 2K_m \ .$$

This choice has been imposed by the limitations of the experiments; it has already been performed by other authors.[3,4,28] In fact, the value of the integrals are not very sensitive to the choice of these cutoffs.

IV. RESULTS AND DISCUSSION

This section is mainly concerned with the scaled behaviors of the light scattering structure factor S and of the corresponding quantity $\hat{S}$ as deduced from the direct observation. The behavior of the typical wave vector K_m will be also discussed and for the very late stages the velocity of interfaces will be compared to the corresponding K_m evolution.

A. S and its scaling properties

Since the works of Chou and Goldburg[3] and Wong and Knobler,[4] the scaling of $S(K,t)$ has been well assessed. Although a detailed study of S was made necessary to compare with $\hat{S}$, it was also of great interest to compare their data to our measurements since we have used a nonclassical experimental procedure.

Tests of scaling are twofold: evolution of the reduced structure factor $F(x,t)$ and of the reduced second moment $r(t)$, which should not vary with time in the case of a perfect scaling behavior.

Some typical structure factors $S(K,t)$ are reported in Fig. 11(a) ($T_c - T_f = 1.5$ mK, t range $= 30-80$ s), together with the reduced factor $F(x,t)$ [Fig. 11(b)]. This latter demonstrates that scaling is indeed verified.

Figure 12 is devoted to the comparison of an average of our F data with those reported in Ref. 4 for the isobutyric acid and water system by Wong and Knobler, and with the theoretical shape [Eq. (14)] proposed by Furukawa. In spite of a few discrepancies, one can consider the agreement as excellent when considering the experimental uncertainties—and especially the subtraction of the background intensity which must be estimated for each picture.

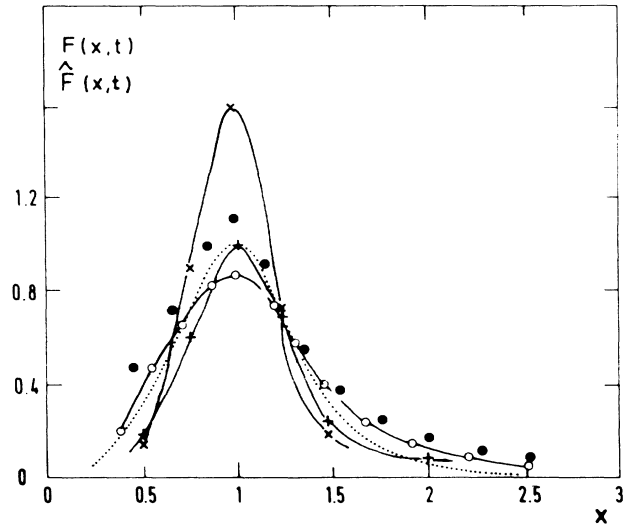

FIG. 12. Comparison between various F-scaled functions. Furukawa's theoretical parametrization (. . .), Chou and Goldburg's data ($\times$), Wong and Knobler's data ($+$), mean value of our $F(x,t)$ data ($\circ$). A mean value of our $\hat{F}(x,t)$ data ($\bullet$) has been reported; although it cannot be compared in principle, it is surprising to find a shape nearly identical to F.

The values of the reduced second moment $r(t)$ are reported in Fig. 13. Scaling is here also well verified and the constancy of r is striking.

As a conclusion to these light scattering studies, the good agreement between our data and those previously reported gives us confidence in the video analysis system.

B. $\hat{S}$ and its scaling properties. Comparison with S

The similar scaled behavior has been found with the reduced structure factor $\hat{F}(x,t)$ deriving from $\hat{S}(K,t)$, as shown in Figs. 14(a) and 14(b) where, respectively, $\hat{S}$ and $\hat{F}$ are shown for a typical quench of $T_c - T_f = 3$ mK.

The comparison of the mean value $\hat{F}$ obtained with all our data and the corresponding F variation is drawn in Fig. 12. Although the similarity between F and $\hat{F}$ is striking, some differences have to be discussed; they are essentially located at low x, where $\hat{F}$ remains larger than F, and at large x, where the tail of $\hat{F}$ is higher than that of F. It is tempting to consider that these differences are significant. However, one must note that close to $K=0$, in both cases, the transmitted light appears as a large peak whose tail makes any measurement uncertain in this region. Similarly, in the large-K region, the background term which has to be removed increases the uncertainty. It is therefore not clear to what extent the differences between F and $\hat{F}$ are meaningful.

The reduced second moment value $\hat{r}(t)$ is found to be a constant (Fig. 13) and its mean value is very close to the corresponding $r(t)$ value obtained by light scattering, $r(t)=1.10\pm0.02$, compared to $\hat{r}(t)=1.11\pm0.02$.

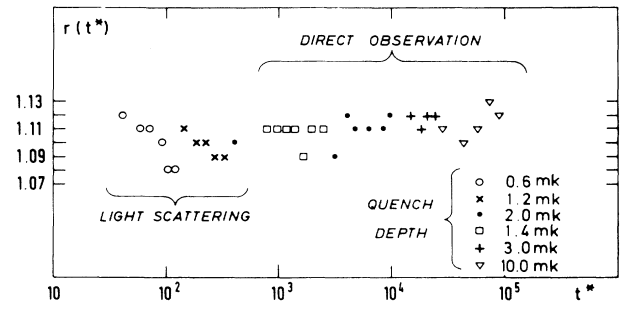

FIG. 13. Evolution of the reduced second moment r vs t^*. The results of six distinct quenches are shown and the analysis was done by light scattering, by direct observation or by both techniques. An average value is around 1.1.

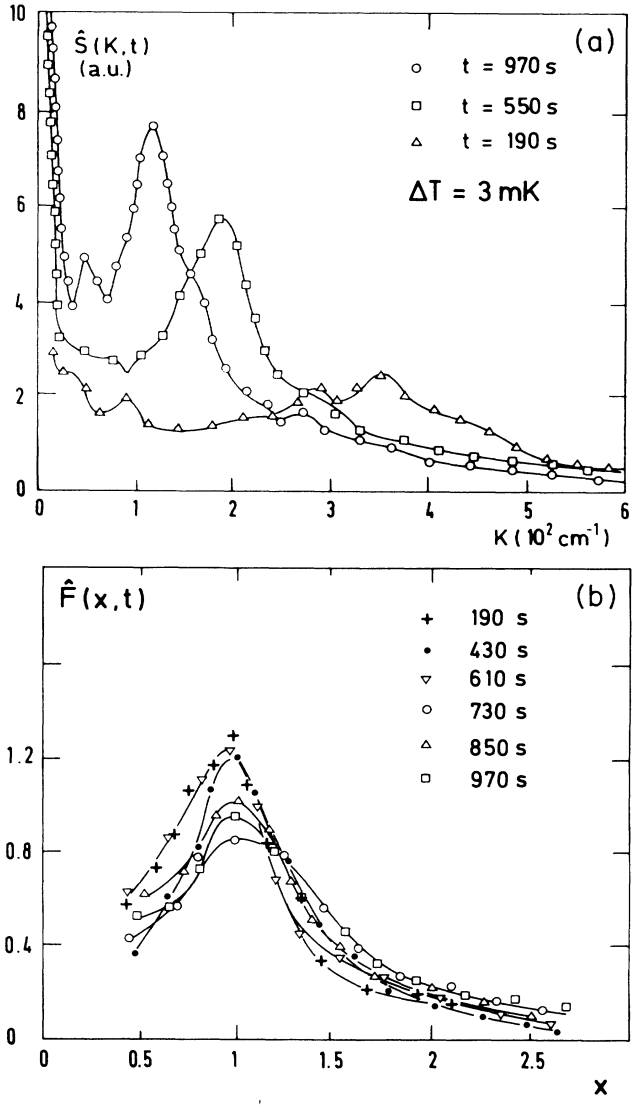

FIG. 14. (a) $\hat{S}(K,t)$ vs K for a 3-mK quench depth (picture analysis). The time elapsed from the beginning of the quench is indicated. (b) Scaling function $\hat{F}(x,t)$ vs x. The different times are indicated.

The value $r(t)=1.14$ can be inferred by using the expression (14) in Eq. (11).

Finally, the important results coming from these analyses concern the strong similarities between the light scattering and the direct-observation methods. One must note also that this latter method allows the study to be performed on a very large time interval, limited only by finite size effects.

C. Behavior of K_m^* versus t^*

The peaks (K_m) of the structure factors S and $\hat{S}$ can be reported on one single curve versus time, provided that the scaled values $K_m^*=K_m\xi^-$ and $t^*=t/\tau^-$ are used. This curve describes merely the temporal evolution of the typical distance $L_m=2\pi/K_m$ between domains (see, e.g., Fig. 8).

In Fig. 15 we have drawn the results we have obtained by light scattering and by direct observation. We have also reported the corresponding values obtained by Chou and Goldburg in the 2,6-lutidine and water system[3] and those obtained by Wong and Knobler in the isobutyric acid and water mixture.[4] They are clearly all in agreement; the values obtained by light scattering and direct observation are especially quite similar. This is consistent with our analysis of the image formation. All our data have been fitted to the analytical variation due to Furukawa [see Eq. (16)].

The resulting values for the parameters A^* and B^* are

$$A^*=0.14\pm0.01 ,$$

$$B^*=0.022\pm0.001 .$$

These values can be compared to those obtained assuming the following mechanisms:

(i) A diffusion-reaction mechanism at small times. In this case $A^*\simeq 2^{1/3}-1=0.26$, which compares favorably with the above value.

(ii) A capillary flow at large time. The constant B has to be evaluated from the estimation by Siggia,[13]

$$K_m^{-1}\simeq B\left[\frac{\sigma}{\eta}\right]t , \tag{29}$$

where B is a numerical constant,

$$B_s\simeq 0.1 .$$

A more refined treatment by San Miguel *et al.*[29] has given

$$B_{\mathrm{SM}}\simeq 0.04 .$$

The numerical comparison of B and B^* can be expressed through the evaluation (2) of the surface tension, and leads to

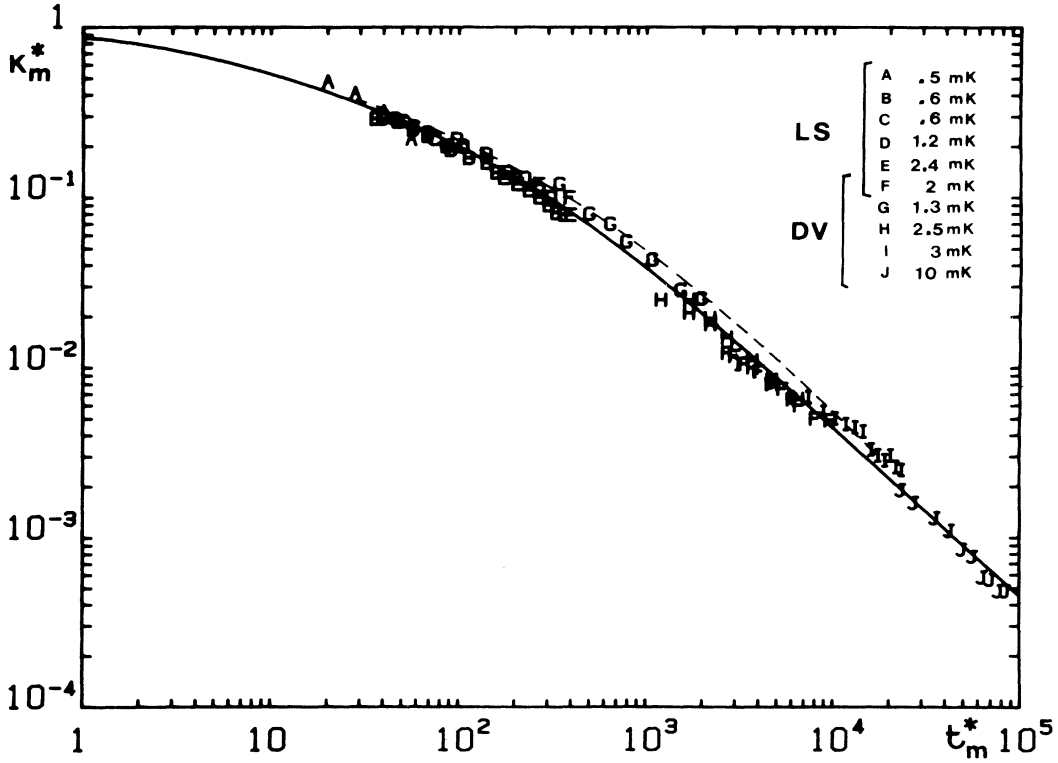

FIG. 15. Plot of K_m^* vs t^*. On this single curve are shown the results obtained by both light scattering (LS) and direct visualization (DV) techniques. A model from Furukawa is drawn with a continuous line. The dashed line corresponds to averaged light scattering measurements [Chou and Goldburg (Ref. 3), Wong-Knobler (Ref. 4)].

$$B^* = \frac{3\pi}{2R} B \simeq 2B \ .$$

The Siggia estimation is far too large, but the constant $B^*_{SM} \approx 0.08$ compares favorably well with our above result.

D. Direct measurement of the interface motion

Looking at the phase-separation pattern gives us the opportunity of measuring directly the velocity at which an interface moves, and thus of determining a value in the exact framework of the theory. At the very end of the phase separation ($t^* \sim 2.10^6$ for $\Delta T_f = 5$ mK), one can observe a phase (M^+), whose typical size is of the order of the cell size, which includes a few domains of the other phase (M^-). These last domains are shrinking with time and a single equilibrium state is obtained when phase (M^+) is surrounded by phase (M^-). The measurement can begin as soon as a definite interface surrounding a domain can be unambiguously delimited.

A measurement of the time evolution of the area $\mathcal{A}$ of a domain gives direct access to the interface velocity. For practical reasons, we have reported the radius (R) of an equivalent disk with the same area $\mathcal{A} = \pi R^2$. The temporal evolution of R (see Fig. 16) allows a global measurement of the interface velocity to be made.

The time dependence of R has been found to be linear,

$$R = R_0 - B_R t$$

with

$$B_R = (2.3 \pm 0.3) \times 10^{-4} \text{ cm s}^{-1} \ .$$

This behavior, which is very comparable to that depicted in Sec. IV C, indicates that the hydrodynamic influence remains strong even at the end of the process. This is shown by the linear variation of R with t which implies a time-independent t interface velocity. The value of B_R leads to a value $B^* \sim 2 \times 10^{-1}$ which is comparable to B^* previously estimated, which implies that the same kind of hydrodynamic instability is operating even at this very late stage.

An interesting point should be the dependence of the interface velocity with respect to the curvature radius. In the case of a system with a nonconserved order parameter (such as an antiferromagnet) it has been shown[30] that the velocity $R(t)$ was directly proportional to $R^{-1}(t)$ which is consistent with the growth law $R(t) \sim t^{1/2}$ which is generally assumed.

In the case of a binary mixture—where the order parameter is conserved—the growth law $R(t) \sim t$ should be consistent with the independence of $R(t)$ upon its curvature radius $R(t)$. The kind of measurement we described above can be used in order to check this point.

V. MORPHOLOGY OF THE PHASE SEPARATION

The most striking signature of a phase separation at criticality is surely its peculiar morphology. The beginning of the phase separation indeed gives birth to a spectacular interconnected pattern (see Fig. 8). Nevertheless, this cannot always be considered as a proof of a spinodal decomposition process, as pointed out by Jantzen and Herman.[31] These authors point out, for instance, that the aggregation of droplets in a nucleation process can also occur in an interconnected way, according to the importance of the volume fraction of the phases in presence.

This is, however, not the case in the above experiments. Within our optical resolution (10 μm), we have always observed the phase separation as developing from interconnected structures, and never from the coalescence of isolated domains.

The final equilibrium state of the system is governed by wetting forces. The methanol-rich phase is preferen-

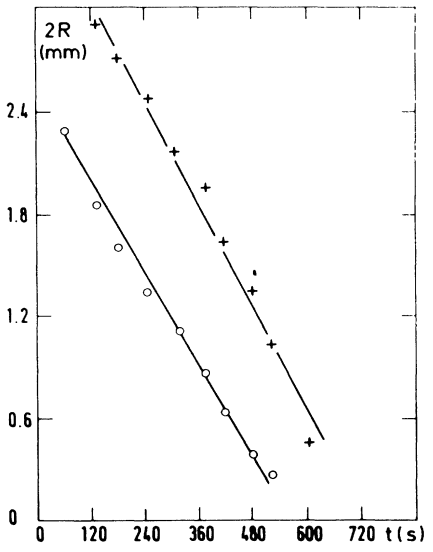

FIG. 16. Experimental measurement of the interface velocity through the evolution of the size (R) of a domain with time t.

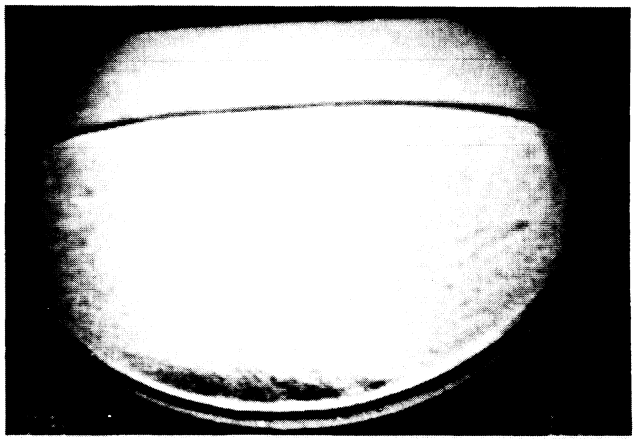

FIG. 17. Total wetting observed at the end of a quench of 5 mK depth ($t^* \sim 3 \times 10^6$). Note the small clusters included in each phase.

tially attracted by the walls and a situation of total wetting is reached. This is actually observed as a macroscopic wetting film which surrounds the nonwetting cyclohexane phase (see Fig. 17).

There remain, however, in both phases small droplets of the complementary phase. They evolve very slowly with time. We interpret this phenomenon by the disconnection of some domains during the growth of the percolated pattern. They are therefore no longer connected and they can grow only by diffusion through the interface. This is a very slow growth mechanism, especially close to the critical point where the mass diffusion is nearly zero.

CONCLUDING REMARKS

The use of an isodensity system has allowed, by rendering negligible the gravity-induced convections and sedimentations, the direct observation of spinodal structures to be performed up to the ultimate stages.

The origin of these images is subtle and resides in allowing the interface pattern to be determined in a plane near the exit window. The fact that on average only one interface out of two is made visible ensures that the interface periodicity is the same as the domain periodicity, and not its double. The problem of connecting the exact shape of the corresponding structure factor to that obtained by light scattering is still open. However, by comparing their statistical properties to the corresponding data obtained by light scattering, it has been shown that these two-dimensional pictures reproduced the scaling properties of the bulk structures and most aspects of their morphology. The scaling properties are seen to remain relevant up to the very end of the phase-separation process.

The study of the morphology of the growth pattern gives evidence of the interconnection of domains as the signature of the phase separation at criticality. Let us note that this coarsening mechanism is very sensitive to the exact criticality of the sample. A slightly noncritical system will exhibit other growth laws[2] which implies that the morphology of the phase separation should be drastically changed as the location of the quench is moved in the phase diagram. A systematic investigation of the different growth morphologies in this phase diagram, with the help of isodensity systems, would be of great interest.

The location of the detectable layer, close to the exit window, should allow surface and wetting properties to be evidenced. Finally, the fact that no gravity influence has been observed during the growth is a good indication that isodensity systems are good candidates to simulate experiments in space. But this is another problem, which is presently under study.[2]

ACKNOWLEDGMENT

We gratefully acknowledge a grant from the Centre National d'Etudes Spatiales (France).

[1]C. Houessou, P. Guenoun, R. Gastaud, F. Perrot, and D. Beysens, Phys. Rev. A **32**, 1818 (1985); D. Beysens, Acta Astron. **12**, 525 (1985).

[2]D. Beysens, P. Guenoun, and F. Perrot (unpublished).

[3]J. S. Huang, W. I. Goldburg, and A. W. Bjerkaas, Phys. Rev. Lett. **32**, 921 (1974); Y. C. Chou and W. I. Goldburg, Phys. Rev. A **20**, 2105 (1979); **23**, 858 (1981).

[4]N. C. Wong and C. M. Knobler, J. Chem. Phys. **69**, 725 (1978); **85**, 1972 (1981); Phys. Rev. A **24**, 3205 (1981).

[5]A recent review is J. D. Gunton, M. San Miguel, and P. S. Sahni, in *Phase Transition and Critical Phenomena,* edited by C. Domb and J. L. Lebowitz (Academic, New York, 1983), Vol. 8, p. 267.

[6]E. Brezin, J. C. Le Guillou, and J. Zinn-Justin, Phys. Lett. **47A**, 285 (1974).

[7]H. Chaar, M. R. Moldover, and J. W. Schmidt, J. Chem. Phys. **85**, 418 (1986).

[8]See, e.g., A. Kumar, M. R. Krishnamurthy, and E. S. R. Gopal, Phys. Rep. **98**, 57 (1983).

[9]See, e.g., B. J. Berne and R. Pecora, *Dynamical Light Scattering* (Wiley, New York, 1976).

[10]J. W. Cahn, J. Chem. Phys. **42**, 93 (1965).

[11]J. S. Langer, M. Bar-on, and H. D. Miller, Phys. Rev. A **11**, 1417 (1975).

[12]K. Kawasaki and T. Ohta, Prog. Theor. Phys. **59**, 362 (1978); **59**, 1406 (1978).

[13]E. D. Siggia, Phys. Rev. A **20**, 595 (1979).

[14]J. W. Cahn and M. R. Moldover (unpublished).

[15]K. Kawasaki and T. Ohta, Physica **118A**, 175 (1983).

[16]K. Binder and D. Stauffer, Phys. Rev. Lett. **33**, 1006 (1974); K. Binder, C. Billotet, and P. Mirold, Z. Phys. B **30**, 183 (1978).

[17]J. W. Cahn, J. Chem. Phys. **66**, 3667 (1976); for a recent review, see *Fundamental Problems in Statistical Mechanics VI,* edited by E. G. D. Cohen (Elsevier, New York, 1985).

[18]See, e.g., J. L. Lebowitz, J. Marro, and M. M. Kalos, Acta Metall. **30**, 297 (1982).

[19]R. Hosemann and J. N. Bagchi, *Direct Analysis of Diffraction by Matter* (North Holland, Amsterdam, 1962).

[20]H. Furukawa, Adv. Phys. **34**, 703 (1985) and references therein.

[21]R. Gastaud, Thèse, Université Paris VI, 1986 (unpublished).

[22]V. Puglielli and N. Ford, Phys. Rev. Lett. **25**, 143 (1970).

[23]See, for instance, D. Beysens, A. Bourgou, and P. Calmettes, Phys. Rev. A **26**, 3598 (1982) and references therein.

[24]G. Bruhat, *Optique* (Masson, Paris, 1965).

[25]F. F. Abraham, Phys. Rev. **53**, 93 (1979).

[26]F. Perrot, R. Gastaud, and D. Beysens (unpublished).

[27]T. Ohta, Ann. Phys. **158**, 31 (1984).

[28]T. Tzumitani and T. Hashimoto, J. Chem. Phys. **83**, 3694 (1985).

[29]M. San Miguel, M. Grant, and J. D. Gunton, Phys. Rev. A **31**, 1001 (1985).

[30]S. M. Allen and J. W. Cahn, Acta Metall. **27**, 1085 (1979).

[31]C. M. F. Jantzen and H. Hermann, in *Phase diagrams: Material Science and Technology,* edited by A. A. Alper (Academic, New York, 1978).

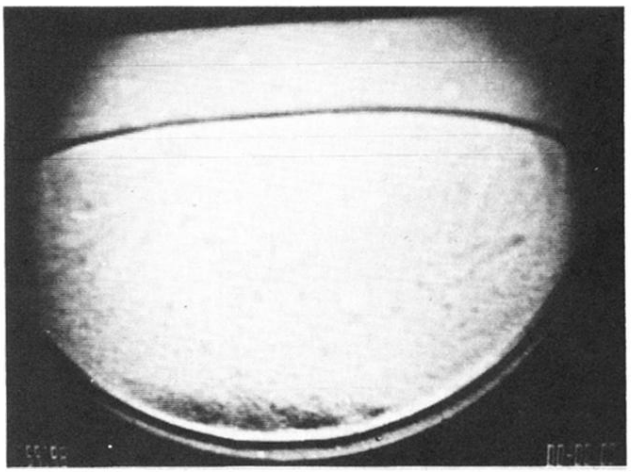

FIG. 17. Total wetting observed at the end of a quench of 5 mK depth ($t^* \sim 3 \times 10^6$). Note the small clusters included in each phase.

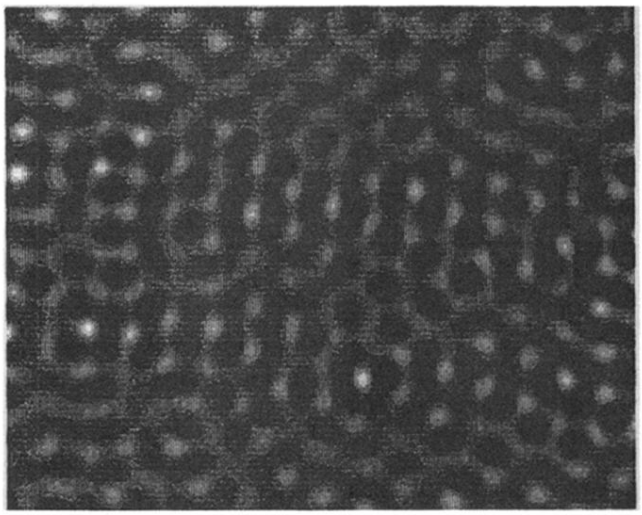

FIG. 3. Numerical simulation of a spinodal decomposition pattern. 20 modes of wavelength having random directions (uniform angular distribution between 0 and 2π), random phases (uniform distribution between 0 and 2π), and random amplitudes according to a Gaussian distribution (64 levels), are added.

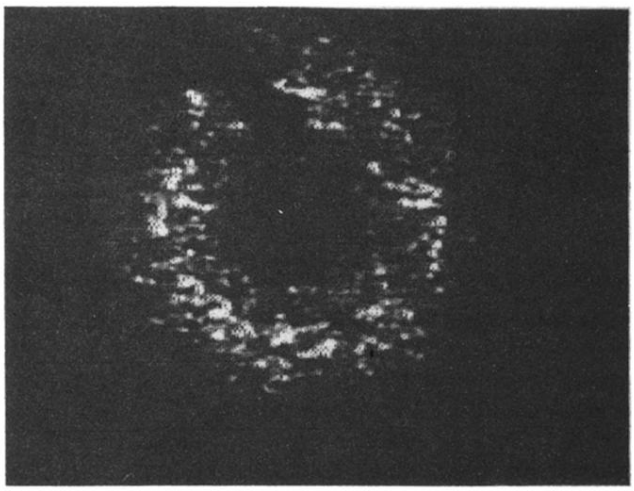

FIG. 5. Typical spinodal decomposition ring obtained by light scattering 70 s after the beginning of the quench ($T_c - T_f = 3$ mK, $K_m = 3.8 \times 10^3$ cm^{-1}, C^*C-M system).

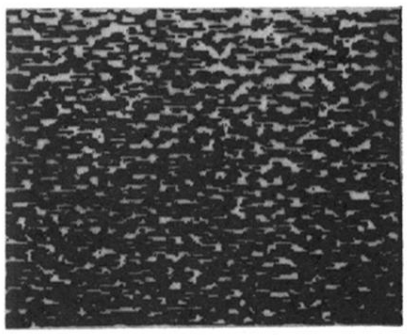

(a)

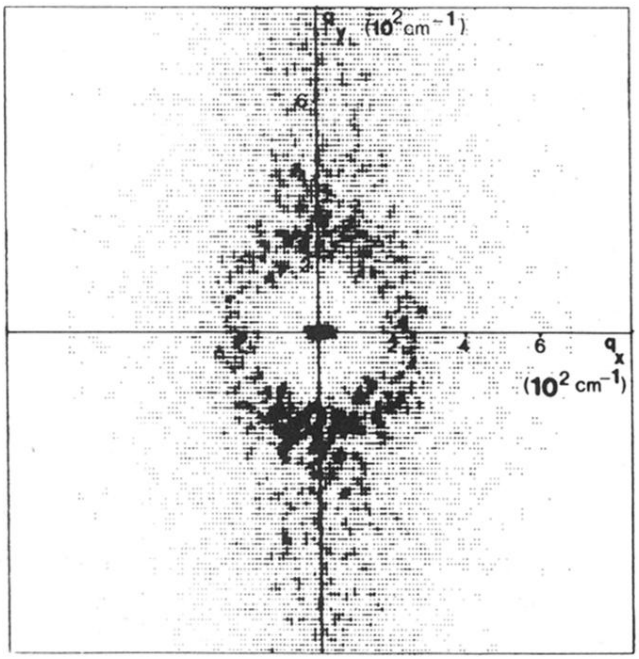

(b)

FIG. 6. (a) Spinodal structures obtained by direct observation. This picture is digitized here only on 5 levels. (b) Structure factor ($\hat{S}$) computed from the structures (a). The radial symmetry is confirmed in spite of a slight asymmetry due to the digitization.

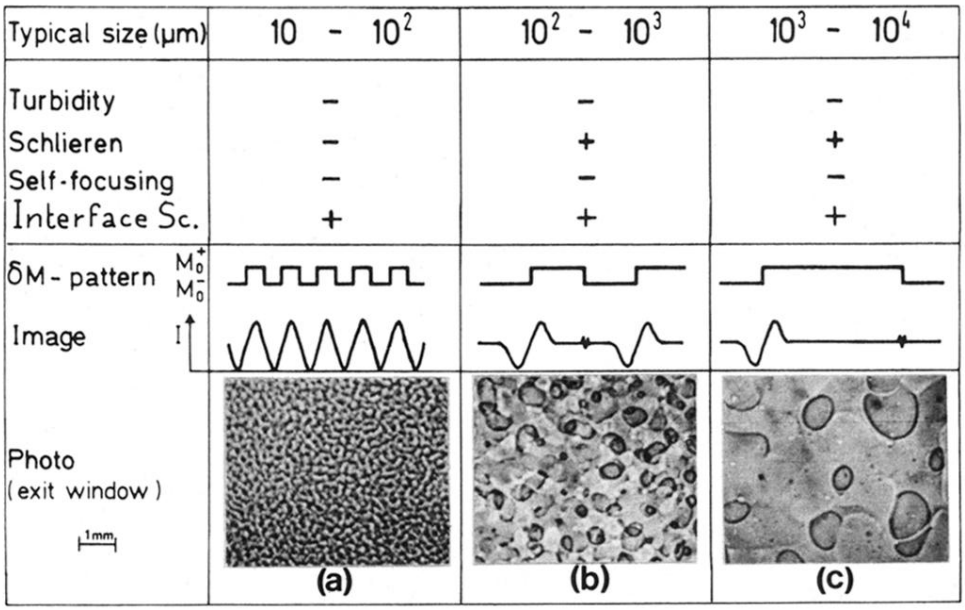

FIG. 8. Presentation of the various optical conditions encountered during the phase separation. For each size the respective influence of the mechanisms is listed, from − (low efficiency) to + (high efficiency).